

Elucidation of Distinct Molecular Resonance Effects in Twist Bend Nematic and Smectic A Liquid Crystals *via* Tender Resonant X-ray Scattering

Yu Cao^{1,2}, Jun Feng², Asritha Nallapaneni^{2,3}, Yuki Arakawa⁴, Keqing Zhao⁵, Feng Liu^{1*}, Chenhui Zhu^{2*}

1 State Key Laboratory for Mechanical Behavior of Materials, Shaanxi International Research Center for Soft Matter, School of Materials Science and Engineering, Xi'an Jiaotong University, Xi'an 710049, P. R. China

2 Advanced Light Source, Lawrence Berkeley National Laboratory, Berkeley, CA 94720 USA

3 Department of Polymer Engineering, University of Akron, Akron, OH 44325 USA

4 Department of Applied Chemistry and Life Science, Graduate School of Engineering, Toyohashi University of Technology, Toyohashi, 441-8580 Japan

5 College of Chemistry, Sichuan Normal University, Chengdu, Sichuan, 610016 China

Abstract Helical structures offer exciting properties and are utilized in numerous applications ranging from biotechnology to displays to medicine. Elucidation of resonance effects in helical structures that provides crucial information on molecular packing beyond positional ordering often remains a challenge due to limited availability of characterization techniques. This limits our understanding of the molecular self-assembly that dictates macroscopic properties. Liquid crystals that are routinely utilized in display industry comprise of helical structures. In this article, we examined the manifestation of resonance effects in twist bend nematic (NTB), smectic A (SmA) and crystalline phases *via* tender resonant X-ray scattering (TReXS) at sulfur K-edge. While SmA layering peak is partially resonant, scattering peak of NTB is purely resonant visible only near S K-edge. The difference is attributed to the periodic molecular orientation variation with weak electron density modulation. We further demonstrate that the energy-dependence of such scattering peak arising from pure orientation variation scales with the sum of $f^2(E)$ and $f'^2(E)$, corresponding to the correction to dispersion and absorption respectively, while the resonant contribution in sulfur-containing SmA scales with $f'(E)$, and is a first order perturbation to the relatively strong non-resonant peak from electron density modulation. We anticipate TReXS will open new avenues in exploration of complex orientational structures in chemistry, biology, and materials science both in static as well as realistic sample environments, such as under mechanical shearing, electric/magnetic field, chemical or optical stimuli.

Self-assembled hierarchical structures have emerged as an important class of advanced functional materials due to their superior optical, mechanical, electrical and hydrophobic properties and are found both in natural and artificial systems. Helical structures, in particular, such as DNA, form the basis of life and are at the core of genetic engineering. Liquid crystals (twist bend nematic - NTB - phase specifically) has garnered significant attention in the recent years due to its fascinating helical structure¹⁻¹³ with potential applications in electro-optical devices¹⁴⁻¹⁷. Formation of helicoidal structures from achiral molecules is one of the prominent features of the NTB phase and helicity is one of the key structural parameters. Broadly speaking, processes that involve symmetry breaking form the core of many natural phenomena and have attracted a lot of interest. These materials are characterized by helical pitch, molecular orientation, bond/orbital ordering of individual chemical bonds and such materials often comprise of rich palette of diverse elements, such as C (carbon), S (sulfur), K (potassium), N (nitrogen), O (oxygen), P (phosphor), Na (sodium), Si (Silicon), etc. Conventional X-ray scattering techniques that rely on spatial electron density fluctuations to provide structural details cannot provide essential information on complex bond orientation or molecular orientation. However, it is crucial to develop an in-depth understanding, e.g. spatial variation of molecular orientation, bond orientation, or molecular orbital orientation, of self-assembly of fundamental building blocks in complex hierarchical structures to advance our current knowledge of the field. This will further enable us to design smart materials with exceptional performance that do not exist in nature.

Resonant X-ray scattering, also known as anomalous X-ray scattering, overcomes the limitations associated with conventional X-ray scattering by taking advantage of the tunable, often enhanced, scattering power near elemental absorption edges and provides important structural information, such as counterion distribution in DNA/protein conjugates^{18, 19}, morphology in multi-component copolymers²⁰, mean molecular orientations at the interfaces of polymer blends^{21, 22}. Tender Resonant X-ray scattering (TRexS) at Sulfur K-edge was successfully applied to discover smectic-C* variants^{23, 24} in the past. Recently, Resonant Soft X-ray scattering (RSoXS) at carbon K-edge has been demonstrated to be a unique and effective tool to directly probe variations in periodic bond orientation in the NTB phase^{25, 26} as well as twisting of periodic layers in the bent-core B4 helical nanofilaments²⁷, nature of double twist cylinders in blue phases,²⁸ and other novel phases²⁹⁻³¹. Despite the promise of utilization of resonant X-ray scattering to decipher orientational order that is beyond mean orientation, the field has largely been unexplored due to limited

access to such instruments and the challenges in data interpretation. Since tender x-ray range covers K-edges (and L-edges) of many important elements such as Na, Mg, P, S, Cl, Si, K, Ti, further development of tender X-ray scattering offers great promise for exploration of complex structures including biomaterials, battery materials, porous metal organic framework, with natural presence of these above elements.

In this letter, we apply TReXS at S K-edge to examine the smectic A (SmA), crystalline and NTB liquid crystal phases, and demonstrate that scattering from NTB and SmA phases exhibit distinct energy dependence, which is further attributed to the differences in their fundamental structures. Specifically, NTB peaks behave as purely resonant owing to pure bond orientation variation, whereas SmA peaks are partially resonant due to layering. Furthermore, we demonstrate that the dramatic intensity variation in NTB scattering peak near S K-edge resonance is driven by the strong energy dependence of complex molecular scattering form factors, $f(E)=f_0+f'(E)+if''(E)$. Our findings will provide a novel route to obtain key structural information related to bond orientation in a broad class of natural/artificial hierarchical materials.

Two kinds of liquid crystals were investigated and their phase sequences are listed in Figure 1. The first one is the cyanobiphenyl (CB) dimers with sulfur atom(s) presenting at the linkers of molecules (CBSnSCB ($n = 7$) and CBSnOCB ($n = 5$ and 7)), exhibiting the NTB phase³². The second material (FBTBT) is newly synthesized according to the reported method³³ exhibiting SmA phase and has sulfur atoms located in the aromatic cores. 4'-Octyl-4-biphenylcarbonitrile (8CB) molecule that possess a rod-like shape as FBTBT but contains no sulfur atoms, was used as a SmA reference. TReXS and absorption spectroscopy measurements were performed at the beamline 5.3.1 at the Advanced Light Source, Lawrence Berkeley National Laboratory. The X-ray beam energy was tuned around the S K-edge, 2472 eV, with a channel cut double-bounce silicon monochromator. A two-dimensional Pilatus detector (300K, Dectris, Inc.) was used to collect the scattering patterns, which were subsequently converted to one-dimensional line profiles using the Nika software package³⁴. The scattering patterns were viewed with Xi-Cam Interface³⁵ at the beamline. The sample-detector distance was tuned between 488 mm and 250 mm to access relevant q range. The beam centers and the sample-to-detector distances were calibrated using silver behenate and 8CB smectic A. X-ray absorption spectra were measured with a photodiode in transmission mode. The practical energy resolution is about 1 eV. To reduce air attenuation, the sample chamber was kept in a helium gas environment.

The NTB phase of CBS7SCB exhibited a single scattering peak at wave vector $q = 0.072 \text{ \AA}^{-1}$, which is only visible near the S K-edge (Fig.2a) and corresponds to the helical pitch of the NTB phase. The helical pitch in all NTB compounds

increased (decrease in the value of q) as the temperature is increased towards the NTB-N transition (Fig.2b). The helical pitch is reversible on heating and cooling. Remarkably, the peak intensity was observed to increase dramatically when the X-ray energy is increased towards the S K-edge (Fig.2a). The peak intensity reduced abruptly right after the S K-edge, which is often simply attributed to the increase in absorption of resonant atoms (SI). All NTB materials examined in this study exhibited strong energy dependence of the scattering peak intensity (SI). This observation is qualitatively similar to the one noticed in NTB in CB7CB^{25, 26} as well as B4 helical nanofilaments in NOBOW²⁷ at C K-edge and NTB in RM1058 at S K-edge³⁶. However, the energy-dependence of such ‘forbidden’ scattering peak originating from periodic bond orientation variation has never been accounted for quantitatively.

The SmA phase of FBTBT, which has two sulfur atoms in the molecular structure, exhibited one peak at $q = 0.214 \text{ \AA}^{-1}$ regardless of the X-ray energy (Fig. 2c) corresponding to a d - spacing ($=2\pi/q$) of 29.3 \AA , which is very close to the extended molecular length (31.3 \AA , obtained using Materials Studio), confirming that this peak has its origin from electron density modulation perpendicular to the plane of the layers. Interestingly, the peak intensity decreased noticeably at the S K-edge. We further measured 8CB containing no sulfur in the SmA phase as a reference to verify that the reduction in intensity is associated with the resonant sulfur atoms. A scattering peak was observed at $q = 0.20 \text{ \AA}^{-1}$, which is in good agreement with the previously reported smectic layer spacing in 8CB³⁷, and the peak intensity remained relatively stable with small fluctuations (Fig. 2d). Clearly, the dip in the SmA peak intensity at S K-edge observed in FBTBT is related to resonant sulfur atoms, although the nature of such behavior seemed fundamentally different from the dramatic increase in NTB peak at S K-edge (Fig. 2a,c).

The crystal phase of FBTBT exhibited several scattering peaks at $35 \text{ }^{\circ}\text{C}$. Notably, the three peaks observed at $q = 0.109 \text{ \AA}^{-1}$, 0.118 \AA^{-1} and 0.131 \AA^{-1} have qualitatively similar energy-dependence as observed in SmA with an intensity dip at S K-edge (Fig. 2e, low angle). The peak observed at $q = 0.325 \text{ \AA}^{-1}$ (Fig. 2e, high angle, the peak on the right) has striking resemblance to the NTB phase and is observed only in the vicinity of S K-edge (SI). The peak present at $q = 0.217 \text{ \AA}^{-1}$ contains mixed features from both the SmA and NTB phases, i.e. the peak is visible even far away from the S K-edge, however, the peak intensity also increased dramatically when approaching the edge. Since the examination of detailed crystal structure is not the primary focus of this work, we will now focus on the more representative energy-dependence behavior in the SmA and NTB phases.

We adapted the scattering intensity expression¹⁸ represented in Eq. 1 to understand the nature of resonant scattering in the NTB and SmA phases, wherein the complex scattering form factor is given by $f(E)=f_0+f'(E)+if''(E)$ and $v(q)$ represents the spatial distribution of resonant species independent of X-ray energy. This expression reveals that

the intensity measured near absorption edge consists of three parts: (1) the first term ($F_0^2(q)$) denotes the non-resonant intensity that is measured from atoms far from their absorption edge; (2) the second term ($2f'(E)F_0(q)v(q)$) corresponds to the cross term of the non-resonant and the resonant part and scales linearly with $f'(E)$; Note that $f'(E)$ is negative and accounts for the reduction in the effective number of electrons whereas the term $f_0+f'(E)$ contributes to scattering (SI). (3) the third term, $(f^2(E) + f'^2(E))v^2(q)$, is based on pure resonant scattering and scales with the sum of $f^2(E)$ and $f'^2(E)$.

$$I_0(q) = F_0^2(q) + 2f'(E)F_0(q)v(q) + (f^2(E) + f'^2(E))v^2(q) \quad \text{Eq. (1)}$$

Based on the experimental data provided in Fig. 2, integrated peak intensity for SmA and NTB phases as a function of X-ray energy was plotted in Fig. 3. Since 8CB contains no sulfur, its molecular form factors should exhibit a negligible dependence on energy around S K-edge, thus the observed small fluctuation in integrated intensity is attributed to background due to beamline optics (Fig. 3b). The SmA in FBTBT shows additional features in integrated intensity, i.e. a sharp intensity dip near S K-edge, besides the small fluctuation seen in 8CB. Clearly, the sharp dip at S K-edge is due to the sulfur atoms present in FBTBT (Fig. 3b). Given a large non-resonant $F_0^2(q)$ term in FBTBT SmA, the cross term in Eq. (1) contains the leading resonant contribution and therefore should be the main perturbation to the measured scattering intensity in Fig. 3b. To calculate the contribution of the cross term quantitatively, X-ray absorption spectra near S K-edge was measured to obtain the imaginary scattering form factor, $f''(E)$ from FBTBT (Fig. 3a) following $\mu = 2\rho N_a r_e \lambda f''/m_a$, where μ is attenuation length, ρ is density, N_a is the Avogadro constant, r_e is the classical electron radius, m_a is the atomic molar mass, and λ is the X-ray wavelength. Evidently, the experimental absorption spectra near the S K-edge (Fig. 3a) differs significantly from the simulation results using Henke atomic scattering factors database³⁸, and the difference is attributed to the well-known limitation of Henke data due to the lack of fine spectral details to describe the absorption and dispersion near absorption edge. In organic molecules, both molecular orbital hybridization and specific local chemical environments, i.e. smectic liquid crystal vs crystalline lattice, affect the details in near-edge absorption spectra. Indeed, absorption spectra was observed to vary among different phases of e.g. SmA and crystalline of FBTBT (SI). The corresponding dispersive component, $f'(E)$, in the SmA of FBTBT, was calculated from $f''(E)$ using Kramers-Kronig relation³⁹, and that overlaps with the measured scattering intensity, $I(E)$, reasonably well (Fig. 3b) indicating a strong evidence that the intensity drop at S K-edge in SmA is due to the second term in Eq. (1), which essentially scales with the energy dependence of the dispersive scattering form factor, $f'(E)$.

In the case of NTB, non-resonant SAXS exhibited no peak at $q = 2\pi/p$, where p corresponds to the full helical pitch, suggesting that the non-resonant term $F_0^2(q)$ in Eq. 1 is negligible. Fig. 3d also indicates that the observed

scattering peak near S K-edge is due to pure resonance, which agrees with the NTB structural model that exhibits periodic bond orientation variation from screw axis. As reported previously, the precise description of bond orientation sensitivity and structure factor calculation typically requires a treatment of a second rank tensorial form factors^{28, 40-42}, which can be modeled as a 3-by-3 matrix but in the simplest case is a diagonal matrix with only two unequal parameters, i.e. scattering form factor parallel, f_{para} , and perpendicular, f_{perp} , to the molecular long axis or specific chemical bond (molecular orbital). Here, we assume a constant anisotropy in the scattering form factor, i.e. a constant ratio of f_{perp}/f_{para} independent of X-ray energy and focus on the general quantitative energy-dependence of such anisotropy, which is responsible for the pure resonant peaks from orientation variation. Complex scattering factor, $f'(E)$ and $f''(E)$ were computed from the measured absorption spectra. Fig. 3d indicates that the computed $f^2(E)+f'^2(E)$ curve matches reasonably well with the measured peak intensity as a function of energy (except for a slight shift in the peak position), thus validating the hypothesis that the energy-dependence of the NTB peak intensity basically follows energy dependence of complex molecular scattering form factors. We note that a similar expression has been adopted for calculating compositional contrast in multicomponent polymeric systems⁴³ but has not been extended to single component systems with strong orientational ordering such as liquid crystals, peptoids and biomaterials.

In conclusion, we have demonstrated distinct resonance effects in the scattering peaks of SmA and NTB phases in Fig 4. In the case of SmA, the leading resonant contribution is essentially a first order perturbation to non-resonant scattering contribution from smectic layering, and it scales with the dispersive correction $f'(E)$. While in the case of NTB, the observed peak is purely resonant originating from periodic orientation variation and the energy-dependence of peak intensity scales with the sum of $f^2(E)$ and $f'^2(E)$. Our findings suggest a novel route to distinguish among pure resonant, partial resonant, and mixed cases quantitatively. The ability to quantitatively separate pure resonant from partial resonant contributions in scattering may provide a unique tool to further investigate the polarization modulated structures in bent-core SmAP_r⁴⁴, the twist grain boundary smectics⁴⁵, and to distinguish between the twist bend nematic and twist splay nematic⁴⁶ phases, the latter of which may involve both periodic orientation variation and electron density modulations. TReXS can be further extended to elucidate the complex hierarchical structures in biomaterials, battery materials, etc.

Resonant X-ray scattering at carbon K-edge has certain advantages especially for organic materials in which carbon is often the main composition. However, utilization of soft X-rays for structural examination is often associated with practical challenges. For example, (a) it requires sample environment to be maintained in a vacuum and sample thickness as thin as hundreds of nanometers due to its low penetration power (e.g. 200 nm attenuation length for

polyimide at 285 eV)³⁸; (b) the existence of multiple carbon atoms in a single organic molecule may pose a limitation to decipher molecular-level interactions. The above complications may be circumvented to some extent by utilizing tender X-rays^{23, 47} or hard X-rays^{48, 49}. Thus, a combination of these tools will open new avenues and offers great promise for exploration of complex orientational structures in chemistry^{50, 51}, biology⁵², and materials science in realistic sample environments, such as under mechanical shearing⁵³, electric/magnetic field, chemical or optical⁵⁴ stimuli.

We thank Dr. Eric Gullikson at CXRO, LBNL, for helpful discussions. We acknowledge use of Beamlines 5.3.1 of the Advanced Light Source supported by the Director of the Office of Science, Office of Basic Energy Sciences, of the U.S. Department of Energy under contract no. DE-AC02-05CH11231. The work is also supported by National Natural Science Foundation of China (51603166 and 21774099), Science and Technology Agency of Shaanxi Province (2016KW-050 and 2018KWZ-03). Y.C. also thanks China Scholarship Council (CSC) for providing financial support (201706280170).

ASSOCIATED CONTENT

Supporting Information. Additional information on TReXS, absorption spectra, atomic form factors, calculations of molecular form factors from measured absorption spectra, integrated peak intensity vs E, are available free of charge via the Internet.

AUTHOR INFORMATION

* Corresponding Author

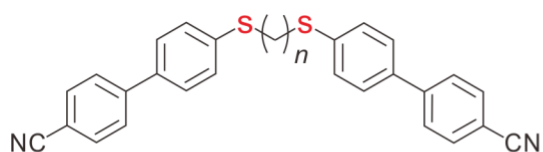
Email: chenhuiizhu@lbl.gov, feng.liu@xjtu.edu.cn

Reference:

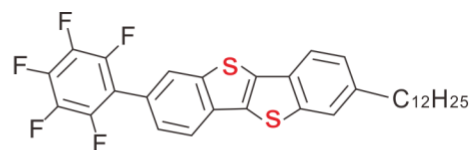
1. D. Chen, J. H. Porada, J. B. Hooper, A. Klitnick, Y. Shen, M. R. Tuchband, E. Korblova, D. Bedrov, D. M. Walba, M. A. Glaser, J. E. MacLennan and N. A. Clark, *Proc Natl Acad Sci U S A* **110** (40), 15931-15936 (2013).
2. V. Borshch, Y. K. Kim, J. Xiang, M. Gao, A. Jakli, V. P. Panov, J. K. Vij, C. T. Imrie, M. G. Tamba, G. H. Mehl and O. D. Lavrentovich, *Nat Commun* **4**, 2635 (2013).
3. P. A. Henderson and C. T. Imrie, *Liquid Crystals* **38** (11-12), 1417 (2011).
4. M. Cestari, S. Diez-Berart, D. A. Dunmur, A. Ferrarini, M. R. de la Fuente, D. J. Jackson, D. O. Lopez, G. R. Luckhurst, M. A. Perez-Jubindo, R. M. Richardson, J. Salud, B. A. Timimi and H. Zimmermann, *Phys Rev E Stat Nonlin Soft Matter Phys* **84** (3 Pt 1), 031704 (2011).
5. R. B. Meyer, *In Molecular Fluids. Les Houches Lectures*. (Gordon and Breach, 1973).
6. I. Dozov, *Europhys. Lett.* **56** (2), 247 (2001).
7. R. Memmer, *Liquid Crystals* **29**, 483-496 (2002).

8. P. J. Barnes, A. G. Douglass, S. K. Heeks and G. R. Luckhurst, *Liquid Crystals* **13** (4), 603-613 (1993).
9. V. P. Panov, M. Nagaraj, J. K. Vij, Y. P. Panarin, A. Kohlmeier, M. G. Tamba, R. A. Lewis and G. H. Mehl, *Phys Rev Lett* **105** (16), 167801 (2010).
10. L. Beguin, J. W. Emsley, M. Lelli, A. Lesage, G. R. Luckhurst, B. A. Timimi and H. Zimmermann, *J Phys Chem B* **116** (27), 7940-7951 (2012).
11. E. G. Virga, *Phys Rev E Stat Nonlin Soft Matter Phys* **89** (5), 052502 (2014).
12. M. Cestari, E. Frezza, A. Ferrarini and G. R. Luckhurst, *Journal of Materials Chemistry* **21** (33), 12303 (2011).
13. C. Greco, G. R. Luckhurst and A. Ferrarini, *Soft Matter* **10** (46), 9318-9323 (2014).
14. J. Xiang, S. V. Shiyonovskii, C. Imrie and O. D. Lavrentovich, *Physical Review Letters* **112**, 217801 (2014).
15. V. P. Panov, R. Balachandran, M. Nagaraj, J. K. Vij, M. G. Tamba, A. Kohlmeier and G. H. Mehl, *Applied Physics Letters* **99** (26), 261903 (2011).
16. V. P. Panov, R. Balachandran, J. K. Vij, M. G. Tamba, A. Kohlmeier and G. H. Mehl, *Applied Physics Letters* **101** (23), 234106 (2012).
17. C. Meyer, G. R. Luckhurst and I. Dozov, *Phys Rev Lett* **111** (6), 067801 (2013).
18. N. Dingenouts, R. Merkle, X. Guo, T. Narayanan, G. Goerigk and M. Ballauff, *J. Appl. Cryst.* **36**, 578 (2003).
19. K. Krishnamoorthy, K. Hoffmann, S. Kewalramani, J. D. Brodin, L. M. Moreau, C. A. Mirkin, M. Olvera de la Cruz and M. J. Bedzyk, *ACS Cent Sci* **4** (3), 378-386 (2018).
20. C. Wang, D. H. Lee, A. Hexemer, M. I. Kim, W. Zhao, H. Hasegawa, H. Ade and T. P. Russell, *Nano Lett* **11** (9), 3906-3911 (2011).
21. B. A. Collins, J. E. Cochran, H. Yan, E. Gann, C. Hub, R. Fink, C. Wang, T. Schuettfort, C. R. McNeill, M. L. Chabinyc and H. Ade, *Nat Mater* **11** (6), 536-543 (2012).
22. J. R. Tumbleston, B. A. Collins, L. Yang, A. C. Stuart, E. Gann, W. Ma, W. You and H. Ade, *Nature Photonics* **8** (5), 385-391 (2014).
23. P. Mach, R. Pindak, A. M. Levelut, P. Barois, H. T. Nguyen, C. C. Huang and L. Furenli, *Physical Review Letters* **81** (5), 1015 (1998).
24. S. Wang, L. Pan, R. Pindak, Z. Q. Liu, H. T. N'guyen and C. C. Huang, *Phys. Rev. Lett.* **104** (2010).
25. C. Zhu, M. R. Tuchband, A. Young, M. Shuai, A. Scarbrough, D. M. Walba, J. E. MacLennan, C. Wang, A. Hexemer and N. A. Clark, *Phys Rev Lett* **116** (14), 147803 (2016).
26. M. R. Tuchband, D. A. Paterson, M. Salamonczyk, V. A. Norman, A. N. Scarbrough, E. Forsyth, E. Garcia, C. Wang, J. M. D. Storey, D. M. Walba, S. Sprunt, A. Jakli, C. Zhu, C. T. Imrie and N. A. Clark, *Proc Natl Acad Sci U S A* **116** (22), 10698-10704 (2019).
27. C. Zhu, C. Wang, A. Young, F. Liu, I. Gunkel, D. Chen, D. Walba, J. MacLennan, N. Clark and A. Hexemer, *Nano Lett* **15** (5), 3420-3424 (2015).
28. M. Salamonczyk, N. Vaupotic, D. Pocięcha, C. Wang, C. Zhu and E. Gorecka, *Soft Matter* **13** (38), 6694-6699 (2017).
29. J. P. Abberley, R. Killah, R. Walker, J. M. D. Storey, C. T. Imrie, M. Salamonczyk, C. Zhu, E. Gorecka and D. Pocięcha, *Nat Commun* **9** (1), 228 (2018).
30. M. Salamonczyk, N. Vaupotic, D. Pocięcha, R. Walker, J. M. D. Storey, C. T. Imrie, C. Wang, C. Zhu and E. Gorecka, *Nat Commun* **10** (1), 1922 (2019).
31. M. T. Murachver, A. Nemati, M. Salamonczyk, C. Bullock, Z. Sabata, H. Rahmani, T. Vorobiova, A. Izadnegahdar, S. M. Salili, V. Norman, C. Zhu, T. Hegmann, S. N. Sprunt, J. T. Gleeson and A. I. Jakli, *Soft Matter* **15** (16), 3283-3290 (2019).
32. Y. Arakawa, K. Komatsu and H. Tsuji, *New Journal of Chemistry* **43** (17), 6786-6793 (2019).
33. H. Monobe, L. An, P. Hu, B.-Q. Wang, K.-Q. Zhao and Y. Shimizu, *Molecular Crystals and Liquid Crystals* **647** (1), 119-126 (2017).
34. J. Ilavsky, *Journal of Applied Crystallography* **45** (2), 324-328 (2012).
35. R. J. Pandolfi, D. B. Allan, E. Arenholz, L. Barroso-Luque, S. I. Campbell, T. A. Caswell, A. Blair, F. De Carlo, S. Fackler, A. P. Fournier, G. Freychet, M. Fukuto, D. Gursoy, Z. Jiang, H. Krishnan, D. Kumar, R. J. Kline, R. Li, C. Liman, S. Marchesini, A. Mehta, A. T. N'Diaye, D. Y. Parkinson, H. Parks, L. A. Pellouchoud, T. Perciano, F. Ren, S. Sahoo, J. Strzalka, D. Sunday, C. J. Tassone, D. Ushizima, S. Venkatakrishnan, K. G. Yager, P. Zwart, J. A. Sethian and A. Hexemer, *J Synchrotron Radiat* **25** (Pt 4), 1261-1270 (2018).
36. M. Salamonczyk, R. J. Mandle, A. Makal, A. Liebman-Pelaez, J. Feng, J. W. Goodby and C. Zhu, *Soft Matter* **14** (48), 9760-9763 (2018).
37. C. Zhu, D. Chen, Y. Shen, C. D. Jones, M. A. Glaser, J. E. MacLennan and N. A. Clark, *Phys Rev E Stat Nonlin Soft Matter Phys* **81** (1 Pt 1), 011704 (2010).
38. B. L. Henke, E. M. Gullikson and J. C. Davis, *Atomic Data and Nuclear Data Tables* **54**, 161 (1993).
39. R. d. L. Kronig, *J. Opt. Soc. Am.* **12** (1926).
40. D. H. Templeton and L. K. Templeton, *Acta Cryst.* **A41**, 133 (1985).

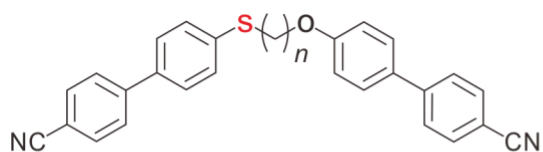
41. A. M. Levelut and B. Pansu, *Physical Review E* **60** (6) (1999).
42. V. A. Belyakov and V. E. Dmitrienko, *Sov. Phys. Usp.* **28**, 535 (1985).
43. T. Araki, H. Ade, J. M. Stubbs, D. C. Sundberg, G. E. Mitchell, J. B. Kortright and A. L. D. Kylcone, *Applied Physics Letters* **89**, 124106 (2006).
44. C. Zhu, R. Shao, R. A. Reddy, D. Chen, Y. Shen, T. Gong, M. A. Glaser, E. Korblova, P. Rudquist, J. E. MacLennan, D. M. Walba and N. A. Clark, *J Am Chem Soc* **134** (23), 9681-9687 (2012).
45. J. Fernsler, L. Hough, R. F. Shao, J. E. MacLennan, L. Navailles, M. Brunet, N. V. Madhusudana, O. Mondain-Monval, C. Boyer, J. Zasadzinski, J. A. Rego, D. M. Walba and N. A. Clark, *Proc Natl Acad Sci U S A* **102** (40), 14191-14196 (2005).
46. A. Mertelj, L. Cmok, N. Sebastián, R. J. Mandle, R. R. Parker, A. C. Whitwood, J. W. Goodby and M. Čopič, *Physical Review X* **8** (4) (2018).
47. H. F. Gleeson and L. S. Hirst, *Chemphyschem* **7** (2), 321-328 (2006).
48. Y. Takanishi, Y. Ohtsuka, Y. Takahashi and A. Iida, *Phys Rev E Stat Nonlin Soft Matter Phys* **81** (1 Pt 1), 011701 (2010).
49. L. S. Hirst, S. J. Watson, H. F. Gleeson, P. Cluzeau, P. Barois, R. Pindak, J. Pitney, A. Cady, P. M. Johnson, C. C. Huang, A. M. Levelut, G. Srajer, J. Pollmann, W. Caliebe, A. Seed, M. R. Herbert, J. W. Goodby and M. Hird, *Phys Rev E Stat Nonlin Soft Matter Phys* **65** (4 Pt 1), 041705 (2002).
50. J. Sun and R. N. Zuckermann, *ACS Nano* **7** (6), 18 (2013).
51. H. Furukawa, K. E. Cordova, M. O'Keeffe and O. M. Yaghi, *Science* **341** (6149), 1230444 (2013).
52. A. Chatterjee, B. Norton-Baker, L. E. Bagge, P. Patel and A. A. Gorodetsky, *Bioinspir Biomim* **13** (4), 045001 (2018).
53. W. Yang, V. R. Sherman, B. Gludovatz, E. Schaible, P. Stewart, R. O. Ritchie and M. A. Meyers, *Nat Commun* **6**, 6649 (2015).
54. D. A. Paterson, J. Xiang, G. Singh, R. Walker, D. M. Agra-Kooijman, A. Martinez-Felipe, M. Gao, J. M. Storey, S. Kumar, O. D. Lavrentovich and C. T. Imrie, *J Am Chem Soc* **138** (16), 5283-5289 (2016).



CBS7SCB: Iso 115.2 N 88.3 NTB 15.9 G

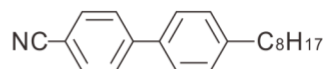


FBTBT: Iso 203 SmA 160 Cr1 40 Cr2*



CBS5OCB: Iso 143.5 N 90.1 NTB 76.6 Cr

CBS7OCB: Iso 146.7 N 95.9 NTB 55 Cr



8CB: Iso 40.4 N 33.4 SmA 21.4 Cr

Figure 1. Molecular structures and phase diagrams of CBSnSCB, CBSnOCB, FBTBT and 8CB molecules, where n is the number of repeating $-\text{CH}_2-$ unit. The dimers CBSnSCB and CBSnOCB were reported to exhibit NTB phase³². Newly synthesized sulfur-containing FBTBT exhibits SmA phase. 8CB without any sulfur was used as a reference for SmA.

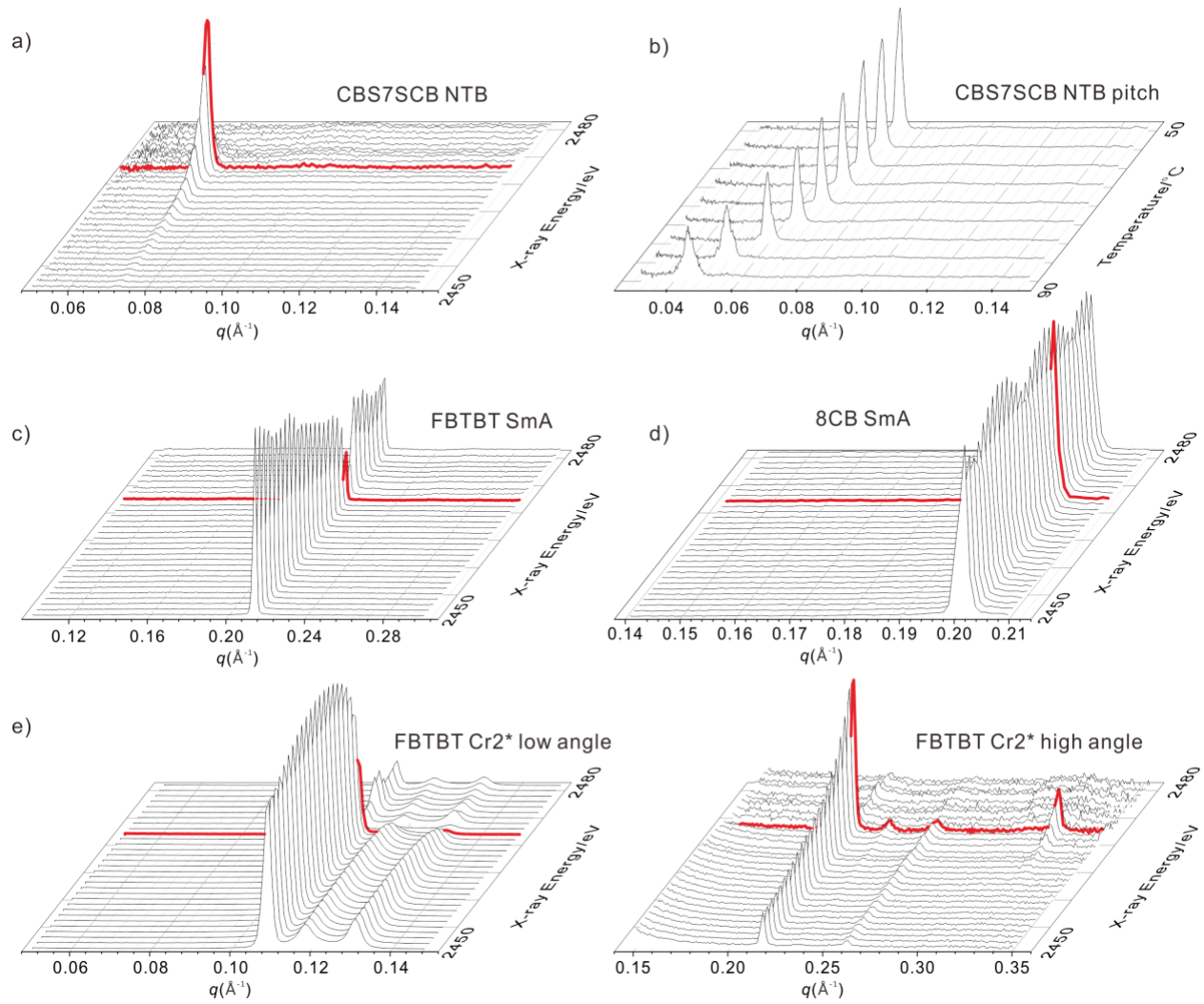


Figure 2. Waterfall plots of (a) TRexS Energy scan of CBS7SCB NTB phase at 60°C indicates the presence of an energy dependent resonant peak at 0.072\AA^{-1} . (b) Temperature scan of NTB phase at 2471eV upon cooling from 90°C to 50°C of CBS7SCB. Pitches decreased upon cooling from the nematic phase. (c), (d) Energy scans of SmA phase of FBTBT (with sulfur atoms) at 195°C and 8CB (without sulfur atoms) at room temperature, respectively. A sudden intensity dip is observed in the vicinity of S K-edge for FBTBT but not for 8CB. (e) Energy scan of FBTBT crystal phase at room temperature. Low and high angle regions were separated so that distinct features can be observed clearly. Peaks at low angle region were visible even far away from the S K-edge and hence considered non-resonant. The peak at 0.325\AA^{-1} is visible only in the vicinity of S K-edge and considered as pure resonant peak. The peak at 0.217\AA^{-1} exhibited combined features of both non-resonant and pure resonant peaks. Red lines correspond to the scattering at $E=2741\text{eV}$, slightly below S K edge.

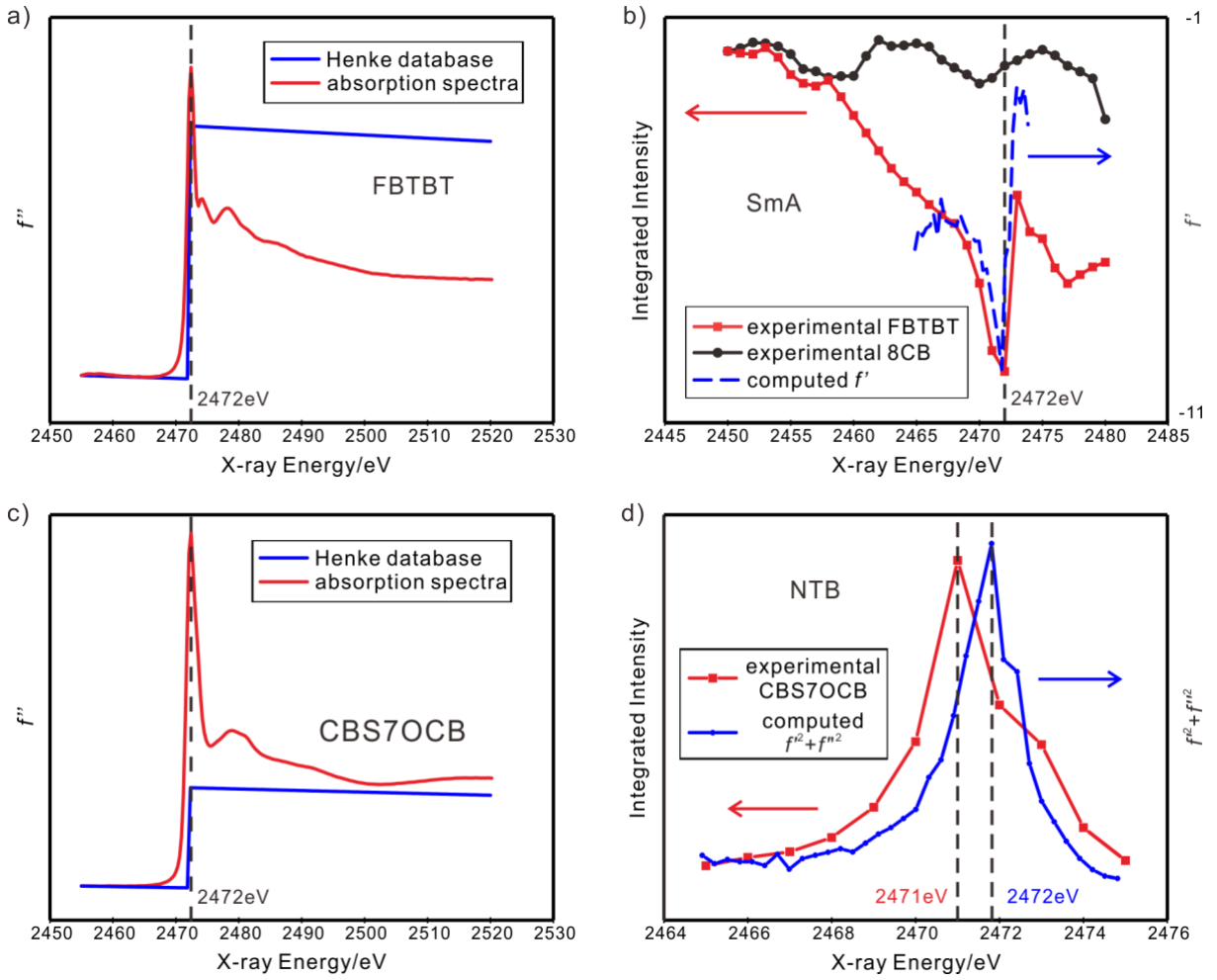


Figure 3. (a) Imaginary scattering form factor (f'') computed from experimental absorption spectra (red) taken in FBTBT SmA phase (at 195°C) and Henke atomic scattering factors database (blue) of FBTBT. Significant differences are observed around sulfur absorption edge (2472 eV). (b) The integrated intensity of SmA peak of 8CB (black), partially resonant SmA peak of FBTBT (red), and computed real dispersion correction (f') (blue dash line) vs X-ray energy. For comparison, intensity of 8CB is scaled using a multiplier constant to match with the intensity of FBTBT at 2450 eV. A dramatic dip around S K-edge can be found for FBTBT from experimental result. The computed f' shows a similar dip at S K-edge suggesting that the intensity dip in FBTBT arises from resonant sulfur atoms. (c) Computed imaginary dispersion correction (f'') from absorption spectra (red) and Henke atomic scattering factors database (blue) of CBS7OCB at 90°C. (d) Computed scattering contrast ($f'^2 + f''^2$) and experimental integrated intensity vs X-ray energy of CBS7OCB NTB phase. Experimental data reaches its maximum at 2471eV with strong energy dependence. Intensity increased dramatically, i.e. by a factor of > 15 from 2464 to 2472eV. Both experimental and computed results exhibit similar trends around absorption edge except for a slight shift attributed to the instrumental resolution limitation.

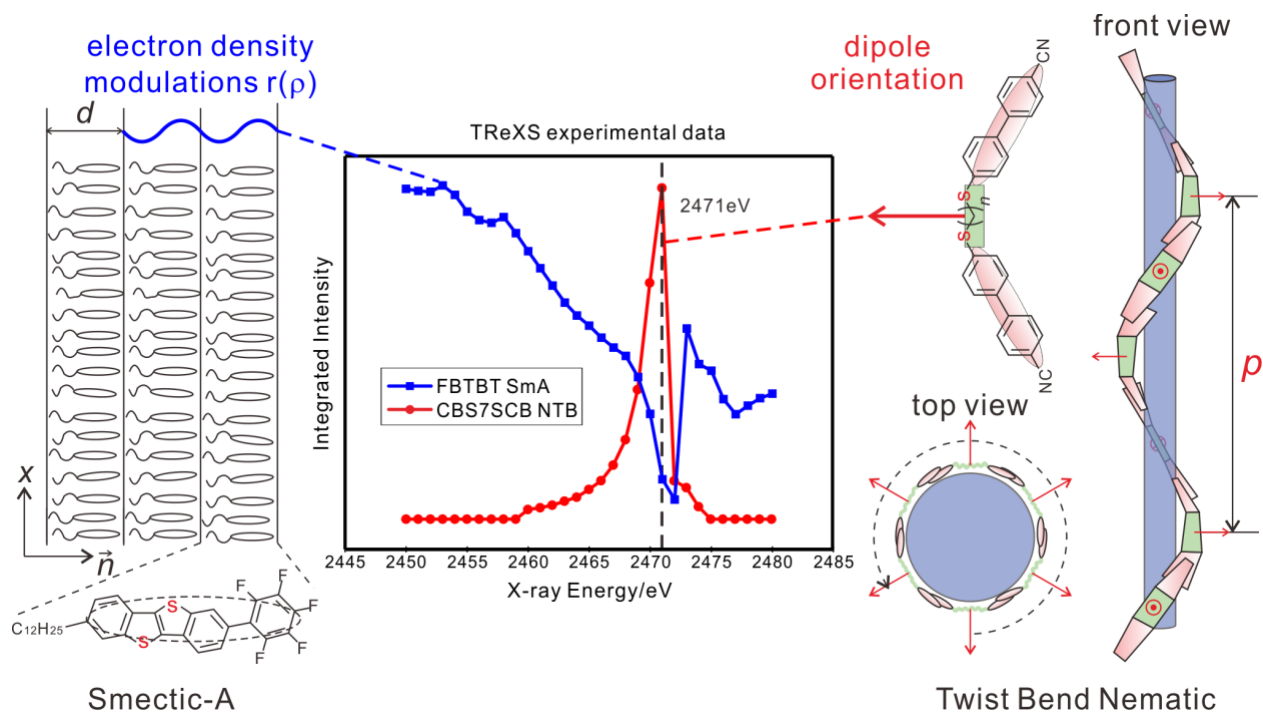


Figure 4. Schematic depicting molecular arrangement in FBTBT SmA phase (left), CBS7SCB NTB phase (right) and the energy dependence of integrated intensity of NTB helix peak (red) and SmA layering peak (blue) from TReXS measurements (middle). The SmA peak, generated from electron density modulation $r(\rho)$, is visible even far away from the S K-edge (blue). Resonant contribution from sulfur atoms in FBTBT manifests itself as a sharp dip at S K-edge. On contrary, pure resonant signal in NTB phase, originating from the periodic rotation of dipoles (red), is visible only in the vicinity of S K-edge.